J Nanopart Res (2013) 15:1574
DOI 10.1007/s11051-013-1574-9

RESEARCH PAPER

Gold nanoparticle aerosols for rodent inhalation and translocation studies

Winfried Möller · Neil Gibson · Marianne Geiser · Suman Pokhrel · Alexander Wenk · Shinji Takenaka · Otmar Schmid · Antonio Bulgheroni · Federica Simonelli · Jan Kozempel · Uwe Holzwarth · Christoph Wigge · Sylvie Eigeldinger-Berthou · Lutz Mädler · Wolfgang G. Kreyling

Received: 15 November 2012 / Accepted: 8 March 2013 / Published online: 19 March 2013

Abstract The intensive use of nano-sized particles in many different applications necessitates studies on their risk assessment as there are still open questions on their safe handling and utilization. For reliable risk assessment, the interaction of nanoparticles (NP) with biological systems after various routes of exposure needs to be investigated using well-characterized NP. We report here on the generation of gold-NP (Au-NP) aerosols for inhalation studies with the spark ignition technique, and their characterization in terms of chemical composition, physical structure, morphology, and specific surface area, and on interaction with lung tissues and lung cells after 1 h inhalation by mice. The originally generated agglomerated Au-NP were converted into compact spherical Au-NP by thermal annealing at 600 °C, providing particles of similar mass, but different size and specific surface area. Since there are currently no translocation data available on inhaled Au-NP in the 10–50 nm diameter range, the emphasis was to generate NP as small as 20 nm for inhalation in rodents. For anticipated in vivo systemic translocation and dosimetry analyses, radiolabeled Au-NP were created by proton irradiating the gold electrodes of the spark generator, thus forming gamma ray emitting ^{195}Au with 186 days half-life, allowing long-term biokinetic studies. The dissolution rate of ^{195}Au from the NP was below detection limits. The highly concentrated, polydisperse Au-NP aerosol ($1–2 \times 10^7$ NP/cm^3) proved to be constant over several hours in terms of its count median mobility diameter, its geometric standard deviation and number concentration. After collection on filters particles can be re-suspended and used for instillation or ingestion studies.

Keywords Gold nanoparticles · Spark ignition · Chain aggregate/agglomerate · Proton irradiation · Au-195 radiolabel · X-ray diffraction

W. Möller (✉) · A. Wenk · S. Takenaka · O. Schmid · W. G. Kreyling
Comprehensive Pneumology Center (CPC), Institute of Lung Biology and Disease (iLBD), Helmholtz Zentrum München—German Research Center for Environmental Health, Ingolstaedter Landstr. 1, 85764 Neuherberg, Munich, Germany
e-mail: moeller@helmholtz-muenchen.de

N. Gibson · A. Bulgheroni · F. Simonelli · J. Kozempel · U. Holzwarth
Institute for Health and Consumer Protection, Joint Research Centre of the European Commission, Via E. Fermi 2749, 21027 Ispra, VA, Italy

M. Geiser · C. Wigge · S. Eigeldinger-Berthou
Institute of Anatomy, University of Bern, Baltzerstrasse 2, 3000 Bern 9, Switzerland

S. Pokhrel · L. Mädler
Department of Production Engineering, Foundation Institute of Materials Science (IWT), University of Bremen, Bremen, Germany

Introduction

Nanoscale particles are widely used in industrial sectors, technology, consumer products, science, and medicine (Seaton and Donaldson 2005; Moghimi et al. 2005; Oberdörster et al. 2005; Maynard et al. 2006; Doane and Burda 2012). Among many recent NP formulations nowadays available gold nanoparticles (Au-NP) have wide applications in science and medicine. The unique surface morphology has allowed various labeling options for cell receptors and cell types including tumor cells (Arvizo et al. 2010; Papasani et al. 2012). In addition, they exhibit light and gamma ray absorption and scattering properties making them novel targets for optical and X-ray enhancement as well as contrast substances (Hainfeld et al. 2006; Rand et al. 2011). However, the safety of NP is mandatory for their use in living organisms including humans.

Many studies suggest that nanometer-sized particles show specific toxicity characteristics in cell systems and living organisms and may follow specific transport and translocation routes in the body, being different from micrometer-sized particles (Donaldson et al. 2004; Oberdörster et al. 2005; Geiser and Kreyling 2010). Materials being non-toxic in the micrometer size range can show toxicity in the nanometer size range (Ferin et al. 1992). In addition, the toxicology metrics of nanomaterials seem not to be mass based but are more related to surface area and particle number. Inhaled nanometer-sized particles may pass into the circulation and be transported to, and accumulate in, secondary organs such as the brain, possibly playing a role in neurodegenerative diseases (Oberdörster et al. 2005; Peters et al. 2006). However, these specific transport properties of NP may also offer new therapeutic opportunities, underpinning the new discipline of nano-medicine in pharmacology (Doane and Burda 2012).

The rapidly developing field of nanotechnology, and in particular the increasing use of NP in various applications, is creating an urgent need for toxicology studies in order to assess and minimize potential health impacts (Nel et al. 2006; George et al. 2010). This holds in particular for inhaled engineered NP. The following aspects need to be addressed:

(1) distribution and transport of NP within the respiratory tract,
(2) their potential to cross the air–blood barrier (ABB) into the circulation and accumulate in secondary organs and tissues,
(3) toxicological responses in the lungs and other tissues to the presence and/or accumulation of NP.

In order to study and understand these mechanisms, well-characterized aerosols of nanometer-sized particles are required and in case of studies of quantitative biokinetics, a stable radiolabel is required. Recently, we have described the generation and characterization of titanium dioxide NP aerosols radiolabeled with ^{48}V using spark ignition aerosol generation technology (Kreyling et al. 2011). The Au-NP described here fulfill all these requirements. Using the spark discharge method, NP can be produced as an aerosol for direct inhalation. Gold can be radiolabeled by neutron or proton bombardment yielding different gold isotopes, such as ^{198}Au or ^{195}Au, which are gamma emitters and can be quantified using gamma ray detectors. Electron microscopic analysis of NP at the individual particle level in tissues or cell cultures is also highly important as it provides information about the cells and intracellular components which are the targets of (inhaled) NP. These analyses contribute to the understanding of underlying mechanisms and the modes of action that may eventually lead to adverse health effects. Prerequisites for such studies include adequate particle application (i.e., inhalation for lung targeting) and tissue preservation, representative tissue and particle sampling for quantitative analysis (unbiased stereology), as well as unambiguous particle identification (Geiser and Kreyling 2010; Kreyling et al. 2013). Recently, we reported on an Au-NP inhalation study, in which we had used thermally untreated Au-NP agglomerates/aggregates (Takenaka et al. 2012). Based on this study, we have further developed our aerosol generation technology, as we describe here. In order to study particle biokinetics in the physiological (non-toxicological) regimen, our studies focused on inhalation studies of only few hours, where no toxicological signs in the lung or other organs could be seen. However since the aerosol is stable over hours and for several consecutive days, long-term exposure studies could be conducted. In addition, particles could be collected on filters and re-suspended for use in ingestion or instillation studies.

Materials and methods

Generation of Au-NP using spark ignition technology and online inhalation

In the aerosol generator (GFG100, Palas, Karlsruhe, Germany) sparks were generated by a high voltage discharge between two adjacent gold rod electrodes in an argon (Ar) gas stream of 3 L/min, as shown in Fig. 1. In this spark ignition process tiny amounts of gold from the tip of the electrode surface evaporate and condense very quickly forming primary liquid clusters which coagulate while cooling, forming solid primary particles. They continue to coagulate into agglomerates bound by weak van der Waal forces, due to the very high particle concentration of $>10^8/cm^3$ until coagulation is virtually stopped by gas dilution and decrease of particle concentration. By altering the frequency of the spark discharge, the resulting mass output and hence the coagulation-driven size distribution of the chain-agglomerated/aggregated NP can be varied. The highly charged aerosol was quasi-neutralized by an inline radioactive ^{85}Kr source about 10 cm^3 downstream of the spark generation chamber. For dilution, the aerosol is mixed with oxygen and nitrogen to obtain an oxygen concentration of 20–25 % at a flow rate of typically 10 L/min. The oxygen/nitrogen mixture was humidified through a semi-permeable tube to achieve a final relative humidity of the aerosol between 70 and 90 %. All aerosol lines were made of metal and they were properly grounded to avoid losses due to NP charge and the release of volatile organic compounds which we have proven when using plastic tubing.

In order to obtain compact spherical Au-NP, the agglomerate aerosol was heated up to 600 °C in a tube furnace (30 cm length) downstream of the Kr-85 neutralizer. The 600 °C heat treatment caused instantaneous melting of the agglomerates, forming single compact particles. Although the melting point of bulk gold is 1,064 °C, there is a significant melting point depression of Au for particles in the nanometer size range (Buffat and Borel 1976). Since the primary particles within the aggregates are only few nanometers in diameter they melt at temperatures of 600–700 °C. Therefore, the generator can provide two different types of aerosol for inhalation studies, being composed either of agglomerates/aggregates of small primary particles or of larger compact spherical particles.

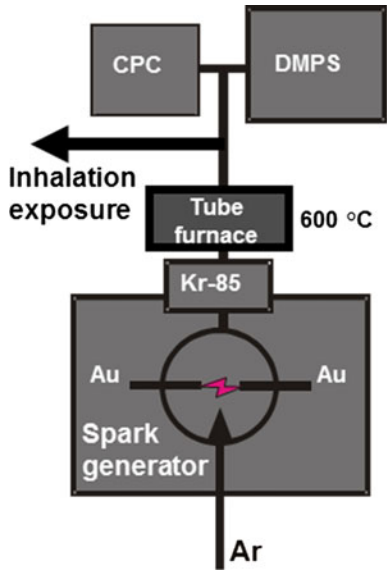

Fig. 1 Set up of spark ignition aerosol generator consisting of Au-electrodes (radiolabeled with ^{195}Au), Kr-85 ion source for aerosol neutralization, a 600 °C tube furnace for particle structure transformation and the aerosol monitoring units (condensation particle counter, CPC and differential mobility particle spectrometer, SMPS). Before Au-NP inhalation by rodents, the aerosol is further diluted using N_2 and O_2 and humidity conditioned

The aerosol was fed through a rodent inhalation apparatus maintained with an absolute filter and pump unit to adjust the aerosol pressure to between 20 and 40 Pa below the laboratory pressure for radiation safety reasons (Alessandrini et al. 2008; Kreyling et al. 2011). Using this system, an aerosol that is stable over several hours is provided to the animals for inhalation within less than 5 s of the initial particle formation. After 1 h Au-NP inhalation by intubated mice, animals were killed and the lungs were processed for electron microscopy as described previously for titanium dioxide aerosol inhalation studies in rats (Geiser et al. 2005, 2008).

Radiolabeling of Au-NP

One end of each of two pure cylindrical gold electrodes (diameter 3 mm, length 4–5 mm) was proton activated in the Scanditronix MC40 cyclotron at JRC Ispra, Italy (Holzwarth et al. 2012). The proton energy was set at a value of 36 MeV. The electrodes were mounted in a closed loop water cooling system with the protons first passing through a 300 μm

aluminium window and about 1–2 mm of water before impinging on the electrode tips, still with an energy high enough to efficiently create ^{195}Hg via the (p,3n) nuclear reaction, together with various other isotopes, including ^{195}Au via the (p,p2n) reaction. The two ^{195}Hg isomers created have half-lives of 41.6 and 9.9 h, so the electrodes were stored after irradiation for several weeks to allow decay of the ^{195}Hg into ^{195}Au. This isotope of gold decays via electron capture into ^{195}Pt with a main gamma emission at 98.9 keV and Pt X-ray emissions at 65.1, 66.8, and 75.8 keV among others (Wilson 1966; Firestone and Ekström 2004). ^{195}Au has a half-life of 186.1 days and thus is ideal for radio-tracing studies over several weeks or months.

The irradiation was carried out over a period of 5 days for a total of 40 h irradiation. The ion beam current was 18 μA, but due to the beam diameter of several mm, only a fraction of the beam actually impinged on the gold electrodes. The depth to which the electrodes were activated was about 500 μm, and the total ^{195}Au activity of the two electrodes after the irradiation and decay period of some weeks was about 50 MBq. A significant activity of ^{196}Au (about 27 MBq) was also present, but this decays with a half-life of 6.2 days, therefore, decreases greatly over several weeks and was negligible during the inhalation studies. A rough estimate of the average ^{195}Au activity concentration in the activated layer gives a value of 370 kBq/mg, but the actual activity concentration would vary somewhat with depth, with a higher activity concentration closer to the surface of the electrodes, tailing off to zero after several hundred microns.

Aerosol size characterization

Aerosol concentration and size distribution were continuously measured using a condensation particle counter (CPC 3022, TSI, Aachen, Germany) and a differential mobility particle size spectrometer (DMPS, consisting of a model 3071 differential mobility analyzer and a model 3010 CPC, TSI, Aachen, Germany), as shown in Fig. 1. The analysis of concentration and particle size was performed at the entry point to the inhalation apparatus in order to ensure correct measurement of the aerosol properties at the time of inhalation. Since the heat-treated Au-NP were solid spherical shaped NP their surface area was calculated using volume determination together with the bulk density of gold.

Au-NP sampling for morphology and chemical analysis

Agglomerate Au-NP (without heat treatment) as well as heat-treated Au-NP were directly deposited onto both silicon wafer substrates and transmission electron microscope (TEM) grids. An electrostatic precipitator (Model 3089, TSI Inc., Aachen, Germany) was connected to the spark ignition aerosol generation system to deposit Au-NP on a 2.5-cm-diameter, single crystalline silicon substrate for chemical and crystallographic analyses. In addition, Au-NP were sampled on formvar-coated copper TEM grids using a bipolar TEM sampler (FHNW bipolar TEM sampler, IAST, University of Applied Sciences of Northwestern Switzerland, Switzerland) (Fierz et al. 2007).

Au-NP morphology and crystalline structure analysis

Conventional TEM, the corresponding selected area electron diffraction patterns (SAED) and high resolution microscopic imaging (HRTEM) of the specimens were investigated using a EM10CR (Zeiss, Oberkochen, Germany) and a FEI Titan 80-300 TEM microscope equipped with a Cs corrector for the objective lens. A Fischione high angle annular dark field detector (HAADF), GATAN post-column imaging filter and a cold field emission gun operated at 300 kV as an acceleration voltage was used (Takenaka et al. 2012). Elemental microanalysis of NP was performed by the energy dispersive spectroscopy (EDX) using the same instrument described above.

Ultrastructural information of NP in three spatial dimensions was evaluated using electron tomography (3D), whereby NP projections acquired from multi-angular tilt series were reconstructed (Baumeister 2002). We performed 3D electron tomography on Au-NP collected from the aerosol line on formvar-coated TEM grids using a Tecnai F20 field emission TEM (FEI Company, Eindhoven, Netherlands) operating at 200 kV. Typical tilt series were acquired at a magnification of 34,000× covering an angular range between −70° and 70° (with an increment of 2°). The pixel size in the tomograms was 0.59 nm. Semi-manual alignment and reconstruction were performed using the

FEI software package (Inspect 3D, Amira, FEI Company, Eindhoven, The Netherlands). For image processing, the ImageJ software equipped with the volume viewer plugin was used.

X-ray diffraction (XRD) of Au-NP for crystalline structure analysis was performed using a PANalytical X'Pert MPD PRO system. The instrument was equipped with Ni-filtered Cu Kα ($\lambda = 0.154$ nm) radiation, ¼° fixed divergence, primary and secondary Soller slit with 0.04 rad aperture, circular sample holder with 16 mm diameter, and X'Celerator detector (position sensitive in a range of 2.122° 2θ with 127 channels, yielding a channel width of 0.01671° 2θ), applying a continuous scan in the range of 15°–140° 2θ and an integration step width of 0.0334° 2θ. The measuring time step was 485 s, to be divided by 127 channels to yield effective measuring time of 3.81 s/0.0334° 2θ. The structural parameters were extracted using Rietveld refinement with the BRASS program. Background, scale factor, unit cell parameters, Gaussian, as well as Lorentzian peak width parameters were simultaneously refined. The structural model (ICSD-52700) for cubic Au was used for refining the X-ray patterns. The quality of the refinement was evaluated in terms of the usual R factor (R_{wp}) and the background corrected residual R'^2_p. A volume-weighted average crystallite size (d_{XRD}) for Au-NP was determined from the line-broadening analysis. The instrumental contribution to the peak broadening was taken into account during the full profile fitting by instrumental parameters derived from a fit of standard crystalline LaB_6.

In addition, samples were analyzed by XRD using a dedicated glancing angle diffractometer designed and constructed at JRC Ispra (Gibson et al. 2000). The system is optimized for analyzing thin films and thus also is ideal for very small sample quantities deposited on Si wafers (Holzwarth et al. 2012). It utilizes Cu Kα radiation, a Soller slit in the diffracted beam, and a solid state detector for background reduction and energy discrimination. The entrance slit can be set to match the chosen incident angle and sample size, and a laser alignment system is used for very accurate sample positioning. The overall angular resolution of the system depends on entrance slit width, but is in the region of 0.15°.

Au-NP analysis in tissue samples

Au-NP TEM analysis in ultrathin tissue sections was performed on chemically fixed lungs (phosphate-buffered 2.5 % glutaraldehyde) after a 1 h inhalation by intubated mice as described for a similar inhalation exposure of rats using titanium dioxide NP aerosols (Geiser et al. 2008). Tissue blocks and cell pellets were further post-fixed with osmium tetroxide and uranyl acetate. Finally, ultrathin sections were stained with heavy metals (uranyl acetate and lead citrate) for conventional TEM analysis using a CM12 TEM (Phillips, Eindhoven, The Netherlands) operating at 80 kV.

Results

Aerosol characterization

For inhalation, the aerosol was further diluted and adjusted to a concentration of 1–3 $\times$ 10^7 NP/cm^3 at a total flow of 10 L/min. Running the spark generator at 150 Hz spark frequency resulted in a 39.2 nm count median mobility diameter (CMD) of the agglomerate/aggregate Au-NP (thermally untreated), whereas after the thermal treatment Au-NP changed to compact 23 nm CMD, as shown in Fig. 2a. The geometric SD was $\sigma_g = 1.6$ both for the untreated agglomerate and the thermally treated spherical particles. The aerosol was constant in size, geometric standard deviation, and number concentration to within ±15 % over several hours per day (Fig. 2b) and even for several consecutive days (data not shown). Mean mass concentrations determined by the weight of filter samples were about 1.6 mg/m^3 (0.9 mg/h).

The specific surface area of the thermally treated Au-NP was calculated to be 13.5 m^2/g for 23 nm diameter spheres, using the density of 19.3 g/cm^3 of bulk gold. The corresponding volumetric specific surface area was 260 m^2/cm^3. Based on TEM measurements of the primary particles of 5–7 nm diameter, there is 3–5 times higher specific surface area of 62 m^2/g for the non-treated agglomerate/aggregate Au-NP, while having the same mass.

The ^{195}Au radioactivity concentration of the aerosol was 1.2 kBq/L at the reference date. Based on radioactivity measurement of an integral filter sample of 0.3 L/min aerosol flow during the entire exposure and the sampled aerosol volume, the aerosol mass concentration was also calculated to be $\approx$1.6 mg/m^3. As would be expected, the ^{195}Au radiolabels were stably integrated into the Au-NP since the radiolabel

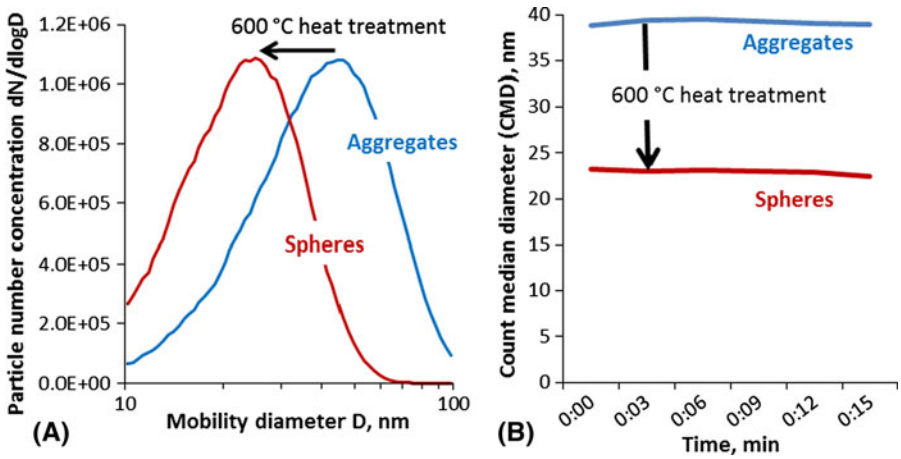

Fig. 2 **a** Particle size distribution of Au-NP after spark ignition generation (*aggregates*) and after additional 600 °C heat treatment (*spheres*). **b** Count median diameter (CMD) before (aggregates, *blue*) and after (*spheres*, *red*) 600 °C heat treatment during 15 min run of the generator system

leaching rate obtained in distilled water by a filter sandwich technique (Kreyling et al. 2011) was below detection limits within the first day.

Au-NP morphology

Transmission electron microscopic analyses revealed that the agglomerate/aggregate Au-NP (as generated, non-heat-treated) consist of almost spherical primary particles of 5–7 nm (geometric) diameter (Figs. 3a, 4). The primary particles are linked into a chain-like agglomerate morphology with a variable length between about ten and several tens of nanometers depending on the direction of measurement. This is consistent with the observed median mobility diameter of 35–40 nm, since for loosely-packed, fractal-like agglomerates as encountered here (fractal dimension is estimated to be 1.5–2.0) the minimum and maximum length of an agglomerate is about 2–3 times smaller and larger than the corresponding mobility diameter, respectively (Baron and Willeke 2001). Comparing the as generated particles with the heat-treated ones it is clear that the sintering (melting) process modifies the internal structure of the particles including their overall morphology, finally forming compact spherical and/or potato-like particles of diameters between 20 and 25 nm (Figs. 3b, 5).

Analysis of the heat-treated aerosol used for inhalation by conventional TEM revealed single Au-NP as well as some agglomerates/aggregates with the majority of the NP in the size range of 20–30 nm geometric diameter. Electron tomography revealed different structural organizations of the heat-treated Au-NP, showing mostly single compact spherical and potato-like particles in addition to agglomerates, as shown in Figs. 5 and 6. Heat-treated Au-NP appear rather compact, in contrast to the loosely arranged spark generated TiO_2-NP agglomerates/aggregates (Kreyling et al. 2011). In the 3D reconstruction (the electron tomogram, Fig. 6), Au-NP appear unconnected to the *xy*-plane (the TEM grid). This is probably due to thickness variations of the formvar support film.

Results of the TEM ultrastructure analysis

The two different types of Au-NP obtained from different preparation techniques were investigated using TEM microscopic imaging. Without heat treatment, the Au-NP were obtained in the long chain-like agglomerated form (see Figs. 3a, 4a) as observed in our previous study (Takenaka et al. 2006, 2012). Although the particles are not sufficiently dispersed, they are crystalline with well-formed lattice planes with neck-to-neck contact. One of the single crystalline particles of the long agglomerate attached to the carbon grid is shown in Fig. 4b. The lattice spacing of this crystalline particle in the (1 1 1) plane was found to be 0.2354 nm which agrees with the highest intensity peak of the Au-NP in the XRD analysis at 38.18 2θ (2.3550 Å; see below and Fig. 8). The high resolution microscopic imaging of the long chain agglomerates and the selected particles from the agglomerate are presented in Fig. 4d, e. The lattice spacing measured at the multiple spots of the agglomerates ranged from 0.234 to 0.238 nm, supporting again phase pure Au-particles. The Au-agglomerates were analyzed using selected area diffraction patterns and the occurrence of the

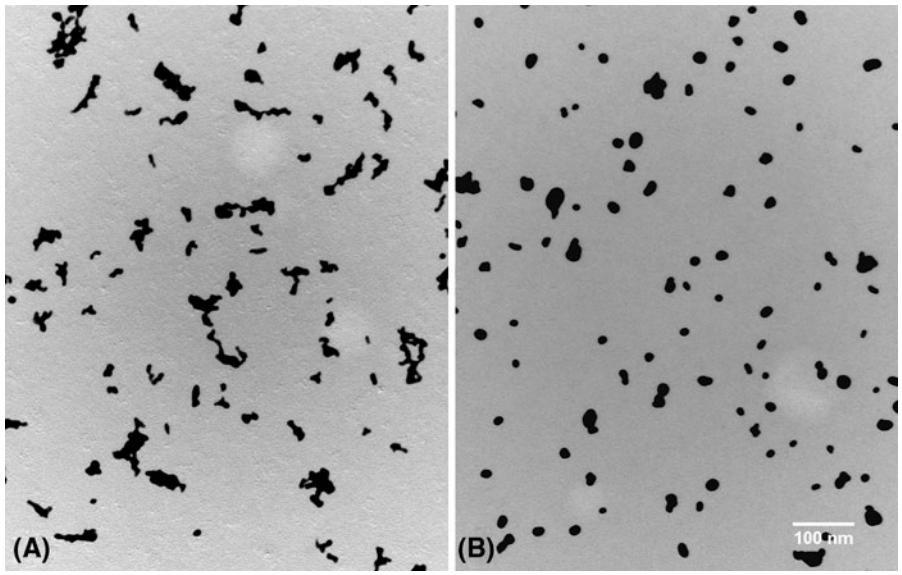

Fig. 3 TEM images of non-heat-treated Au-agglomerates/aggregates (**a**) and of 600 °C heat-treated Au-NP of compact *spherical* and *potato-like* shape (**b**). The *scale bar* holds for both TEM images

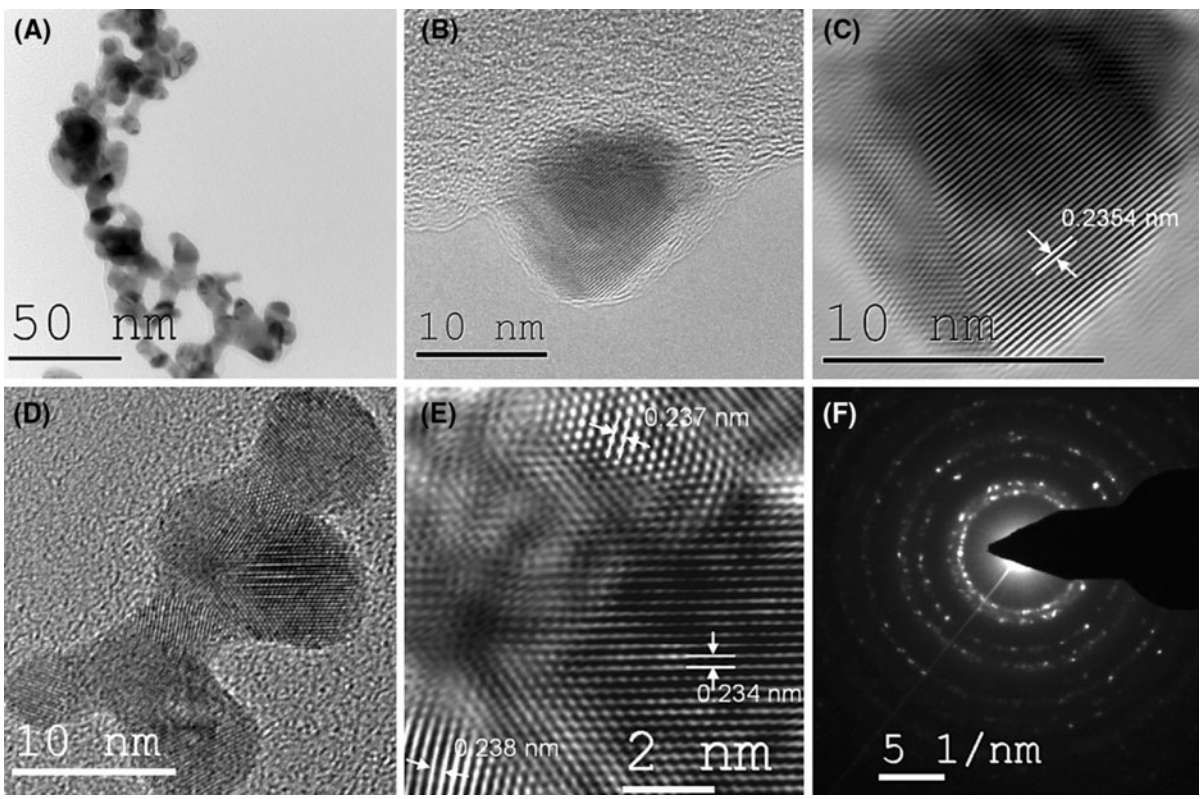

Fig. 4 TEM ultrastructure investigation of the Au-agglomerates before heat treatment. **a** Overview of the particles, **b** a crystalline particle on the edge of the carbon grid, **c** Fourier filtered image of the gold particle, **d** HRTEM image of a large crystalline agglomerate, **e** lattice spacing of the crystalline particle, and **f** selected area diffraction pattern

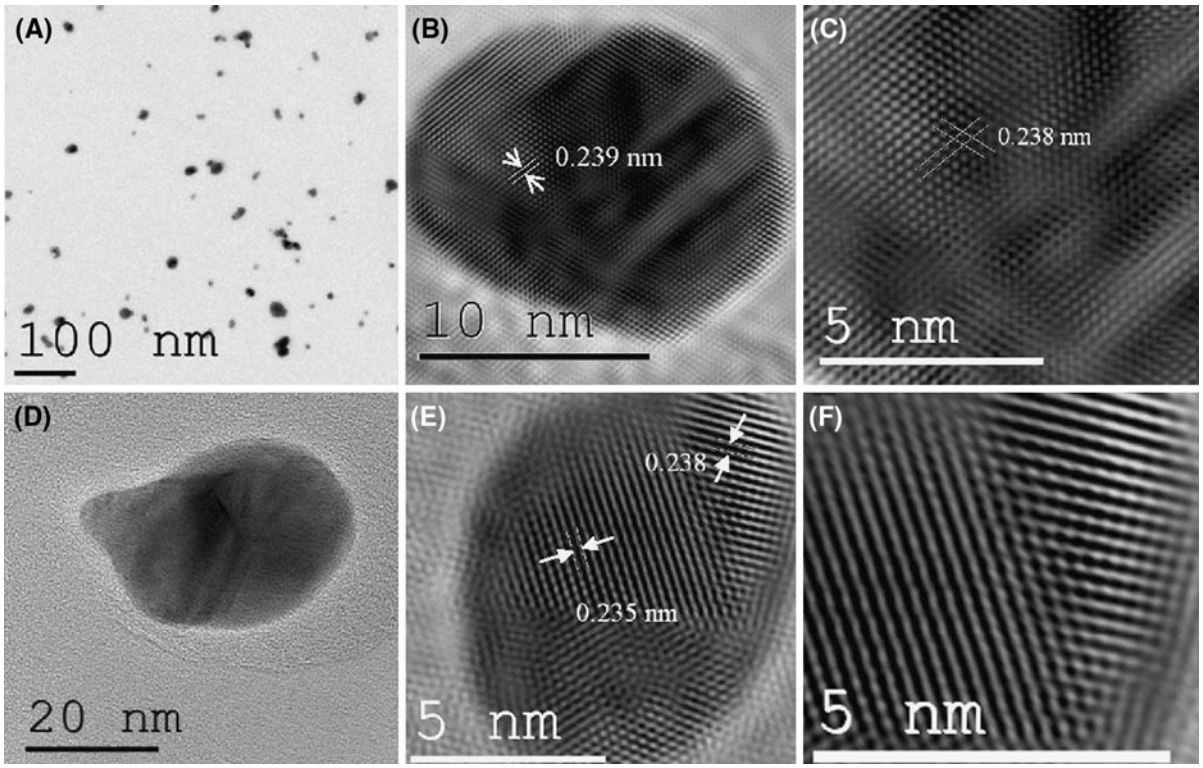

Fig. 5 TEM ultrastructure investigation of the Au crystals after 600 °C heat treatment. **a** Overview of the crystals, **b**, **c** Fourier transformed HRTEM image, **d** overview of a spherical gold particles, **e** high resolution image of the gold spheres, and **f** lattice spacings. Like the agglomerates, gold crystals also have lattice spacings of 2.35–2.38 Å, which agrees with the X-ray data

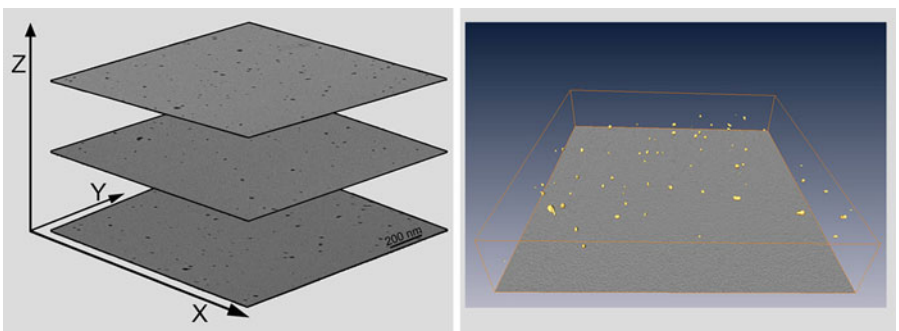

Fig. 6 TEM images and reconstructed electron tomogram of Au-NP. The tilt series consisted of projection images obtained between −70° and 70° tilt angle with an evenly spaced increment of 2°. The magnification was ×34,000. *Topmost, middle*, and *lowest* images of the tomographic reconstruction are shown on the *left*. The 3D reconstruction of the Au-NP (in gold) and the *bottom* image of the electron tomogram are shown on the *right*

crystallographic rings show the high crystallinity of the particles (Fig. 4f).

After in situ heat treatment of these Au-NP at 600 °C, the primary Au-aggregates melted and formed compact spherical and/or potato-like Au-NP. The particles were well dispersed on the TEM grid (see Figs. 3, 5a) ranging from 10 to 30 nm in diameter. The magnified and Fourier transformed image of a particle observed in Fig. 5a is shown in Fig. 5b. The Au crystallite size was found to ranging from 10 to 25 nm

in diameter with a well-formed lattice, suggesting, that the larger particles may be poly-crystalline. The hexagonal arrangement (in the form of dark or bright spots) was also observed within the crystal. The lattice spacing in the (1 1 1) plane and the hexagonal arrangement (two crossed directions) were found to be 2.39 and 2.38 Å, respectively; characteristic of Au-particles (see Fig. 5b, c). The investigation of the particle morphology in different spots revealed that the particles were spherical or potato-like in the size range of 10–30 nm (see Fig. 5d). These Au-particles were also found to be single or poly-crystalline with a similar lattice spacing (2.35–2.38 Å) as described above (see Fig. 5e, f).

The EDX analysis of the untreated agglomerated/aggregated Au-NP and heat-treated Au-NP are presented in Fig. 7a, b. The elemental identification in the wide spot and the single particle scanning shows that the particle contains only Au. The Cu peaks observed in the spectra are due to the Cu grid used for the TEM imaging. The Cl peaks indicated in the spectra are at the noise level so there is no evidence for the presence of chlorine. In summary, the X-ray analysis showed phase pure gold particles with an average size (mass average) of approximately 20–27 nm.

X-ray diffraction results

Figure 8 shows a glancing angle X-ray diffraction (GAXRD) pattern of heat-treated Au-NP deposited on a single crystalline Si substrate. The reference line spectrum is that of gold (JCPDS reference 4–784). The peaks observed support phase pure and well-crystallized Au-NP. The crystalline structure determined on the PANalytical instrument is cubic ($a = b = c =$ 4.064284 Å, $V = 67.14$ Å^3; $Z = 4$) with the FM-$3M$ space group which agrees reasonably with the cell parameters reported in the database. The crystallite size (d_{XRD}) obtained for heat-treated Au-NP determined from the line-broadening analysis was found to be 27 nm for the scan taken on the PANalytical system, while the measurements on the dedicated glancing angle diffractometer showed broader peaks indicating an average crystallite size of approximately 12–15 nm. This size range corresponds very well with the poly-crystallite appearance of the potato-like NP in Figs. 3b and 5.

Inhaled Au-NP in lung tissue

There were no signs of inflammation or toxicity in the lung tissue after the 1 h exposure to the heat-treated Au-NP. Together with the knowledge of Au-NP morphology obtained from the analyses of the TEM grids by conventional TEM and electron tomography described above, Au-NP were identified in ultrathin tissue sections without difficulty. Their well-defined shape, the contrast and the abrupt contrast transition at the particles' edges allows unambiguous particle identification and, hence, does not require any further elemental microanalysis, e.g., by energy filtering TEM (EFTEM). Inhaled Au-NP localized within lung cells were found as single particles or agglomerates of various sizes. Au-NP were primarily located in vesicles, as shown for a lung surface macrophage in Fig. 9, 24 h after Au-NP inhalation.

Discussion

Recently, we reported on an Au-NP inhalation study in which we had used thermally untreated agglomerate/aggregate Au-NP (Takenaka et al. 2006, 2012). Based on these studies, we have further developed our aerosol generation technology in order to produce radiolabeled compact Au-NP, which we describe here.

The described spark ignition generator is capable of providing $\sim$20 nm Au-NP aerosols at high particle number concentration of 1–3 $\times$ 10^7 NP/cm^3 with a lognormal size distribution (median mobility diameter 20–25 nm and a geometric SD of 1.6) and the mass concentration was $\sim$1.6 mg/m^3. This number concentration is the upper limit above which diffusional coagulation is likely to modify the size distribution and number concentration within seconds. Therefore, the inhalation was set up immediately after particle generation. In our pervious study using agglomerate/aggregate Au-NP inhalation lower number concentration of only 4 $\times$ 10^6 NP/cm^3 was chosen with 16 nm mobility diameter (Takenaka et al. 2006). The chain-like structure of the non-heat-treated aerosol was also present in this study, but because of lower number concentration there were many single primary 5–7 nm particles present in the previous study.

The aerosol production was stable over several hours and for several consecutive days. The freshly produced NP aerosols may be used within a few

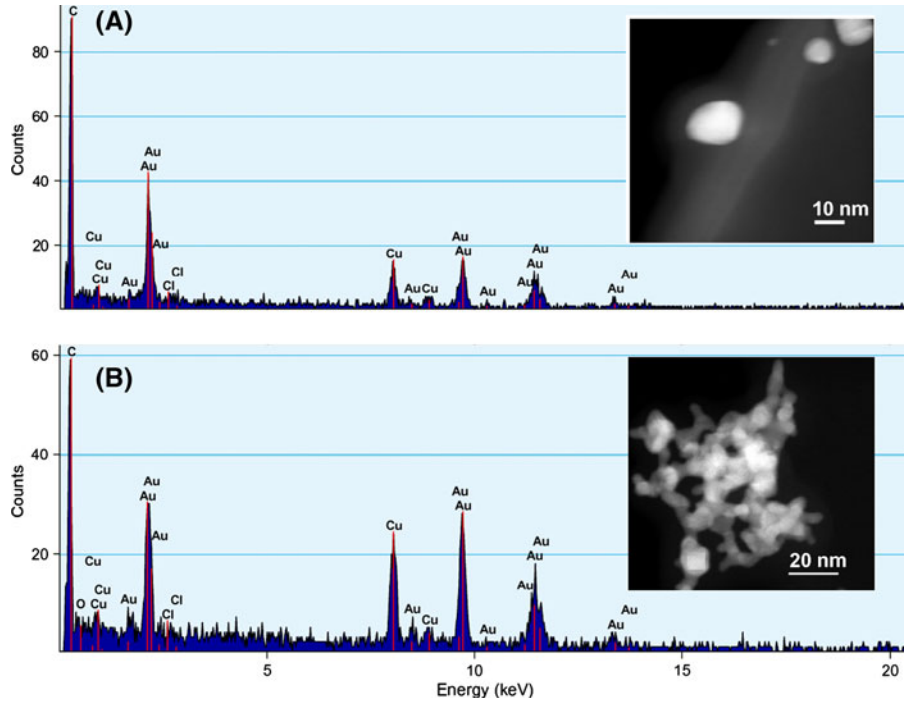

Fig. 7 EDX analysis of **a** the heat-treated spherical Au-NP and **b** non-treated agglomerated/aggregated Au-NP. The *wide spot* and single particle analysis confirm that all the particles/agglomerates are pure gold

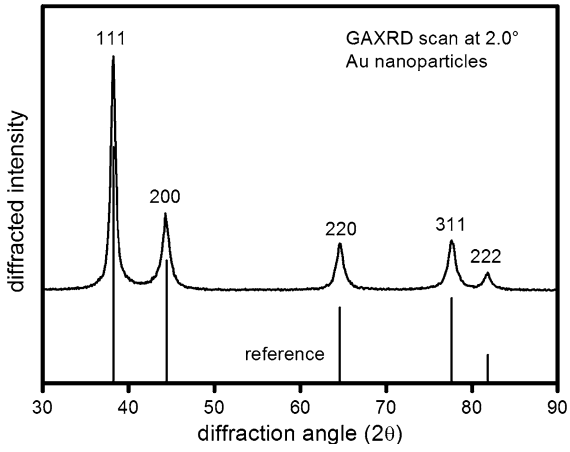

Fig. 8 Glancing angle XRD pattern of Au-NP deposited on a single crystal Si substrate. The *reference lines* are those of JCPDS ref. 4–784

seconds for inhalation experiments in rodents in order to specifically study deposition of these very small particles in the respiratory tract and their interactions with lung tissues. Such small-sized NP aerosols for inhalation can usually not be achieved when dispersing NP powders since the powder cannot be completely dis-aggregated and the particles remain as sub-micrometer-sized agglomerates/aggregates (Ma-Hock et al. 2007). Other techniques for studying NP biokinetics in the lung use intratracheal instillation of a NP suspension (Semmler-Behnke et al. 2008).

Nano particles suspension instillation has the advantage that a known dose is transferred into the lung allowing dose response studies on biokinetics and toxicology. However, there are also several major disadvantages, since a single bolus of a high dose is instilled at one time into the lung, which cannot be achieved during inhalation over several hours. Therefore, the extremely high dose rate and the aqueous volume of the suspension may imply adverse reactions to the lung tissue and non-physiological conditions. In addition, since NP suspensions do usually not contain single NP, but NP agglomerates (Porter et al. 2008), the principle concept of whether NP dispersion instillation studies can mimic NP inhalation exposure is questionable.

Hence, the spark ignition particle generation methodology allows biomedical and toxicological studies with focus on the interactions of the smallest NP with respiratory tract tissues and subsequently, after passing the ABB and transport via blood circulation, with tissues of secondary organs. This is a field which is largely unknown despite the fact that the increasing

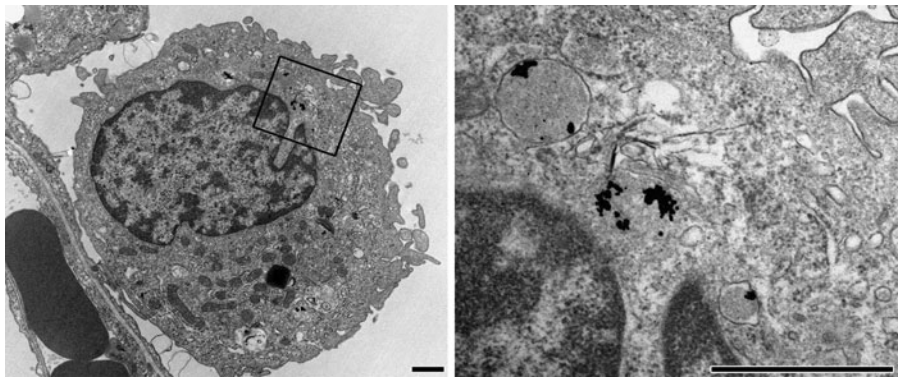

Fig. 9 Ultrastructural analysis of heat-treated Au-NP in lung tissue (*left*). Single or agglomerated Au-NP in vesicles of a lung surface macrophage (*right*). *Bars* 1 μm

use of new types of engineered NP should imply risk and safety assessments of these particles.

Nano particles were characterized very thoroughly for their aerosol characteristics and physico-chemical properties. Spark ignition generation with or without subsequent heat treatment allows the production of two different types of NP, namely agglomerate/aggregate NP and compact spherical NP with similar particle masses. Since the agglomerate/aggregate NP consist of various much smaller primary particles of 5–7 nm diameter (Takenaka et al. 2006; Liu et al. 2012), they differ significantly in their morphological structure and surface area. Because of the high density of gold (19.3 g/cm^3), there is a threefold to fivefold decrease of specific surface area after heat treatment of the Au-NP. Previous toxicology studies gave evidence for the specific surface area to be the major determinant in particle toxicology and not the mass (Stoeger et al. 2006; Oberdörster et al. 2005), and for a threshold surface area above which the organism shows adverse responses. It is expected that the surface area determines the major mechanisms of interaction of the NP with the environment within biological systems (Nel et al. 2009), such as surfactant coating, NP-protein interactions and subsequent transport and translocation processes across cellular membranes and barriers, such as the ABB or the blood–brain barrier (BBB) (Kreuter 2004). Therefore, while delivering similar masses within an inhalation study significantly different surface areas can be applied allowing direct study of these influences.

Proper melting of the non-heat-treated agglomerate aerosol consisting of 5–7 nm primary particles at 600 °C, far below of the melting point of bulk gold (1,064 °C), was also shown in a previous study (Liu et al. 2012), but the authors do not report on particle morphology and crystal structure. In our study, both the primary particles of the Au-NP agglomerates and the heat-treated (melted) spherical Au-NP show the crystal structure of bulk gold with no amorphous component. This may suggest similar internal structure and surface properties of the particles (beyond effects due to decreasing particle size). Therefore, chemical stability and interactions in biological systems and possible coating by proteins in nanomedicine applications may be comparable in both particle types.

For NP radiolabeling, proton irradiation of the gold electrodes at a cyclotron caused a nuclear reaction by which ^{195}Au isotopes were created only in the electrode tips. During spark ignition, ^{195}Au isotopes evaporated together with stable Au atoms from the surface of the electrode and condensed to primary Au-particles. The ^{195}Au-NP aerosol yielded a specific activity of 1.2 MBq/m^3 and 0.75 MBq/mg NP mass. Since only the tip of the gold electrode is activated the specific ^{195}Au radioactivity may decreases during erosion of the first few milligrams of Au of the gold electrodes, resulting in a decrease of specific ^{195}Au activity of the NP aerosol. However, at the aerosol mass concentration of about 1.6 mg/m^3 produced at a total aerosol flow rate of 10 L/min, about 1 h of continuous aerosol operation is required to erode each mg; therefore, major changes would only occur after more than 30 rodent exposures lasting 1 h each.

The estimated deposited dose after 1 h Au-NP inhalation of the aerosol with a mass concentration of 1.6 mg/m^3, assuming a respiratory minute volume

(RMV) of 0.04 L/min (Kuehl et al. 2012) and a deposition fraction of 0.35 of the inhaled aerosol is 1–2 μg. This Au-NP dose did not show any apparent toxicological signs in the lungs of the animals. Therefore, it can be assumed that the particle biokinetics happens under physiological (healthy) conditions. The deposited dose after this 1 h inhalation is by orders of magnitudes lower compared to other toxicological studies, which usually use single bolus instillation of micron- or nanometer-sized particles (Kreyling et al. 2013). Particle identification in the various lung compartments and lung cells after inhalation was previously described for Ir- or TiO_2-NP (Geiser and Kreyling 2010), but the specific distribution and biokinetics of the Au-NP used in this study needs further investigation.

However, for use in medicine thorough toxicology of Au-NP has to be evaluated, i.e., the successful use of Au-NP as X-ray contrast agent in pre-clinical animal studies required much higher doses (10 mg/mL blood) (Hainfeld et al. 2006) as used in our study (2 μg), and the stability of the Au-NP in the organism and possible accumulation in secondary organs may prevent the application in humans. Since toxicology of nanomaterials seems to be primarily related to the specific surface area, including conduction band energy levels (Zhang et al. 2012), and not to the mass, the particles described here are suitable for such hypothesis testing, because particles with similar mass but different specific surface area can be produced. In addition, toxicological reactions have to be expected when the delivered dose (surface area) exceeds certain threshold values (Stoeger et al. 2006). Higher exposure doses can easily be produced by longer exposure times, including accumulating exposures over days and weeks and other than inhalation exposure is possible after particle collection on filters and re-suspension in a medium.

Summary

Spark ignition technology has been used for reproducible production of highly concentrated polydisperse Au-NP aerosols (1–3 $\times$ 10^7 NP/cm^3; $\sim$1.6 mg/m^3, $\sim$0.9 mg/h) which proved to be constant over several hours in terms of their CMD, geometric standard deviation and number concentration. Either chain aggregate/agglomerate Au-NP or compact spherical Au-NP were produced, respectively, without or with 600 °C heat treatment of the aerosol downstream of the spark ignition generator. The Au-NP were extensively characterized in terms of their chemical composition, physical structure, morphology, and specific surface area. Gamma emitting Au-NP were produced with long half-life of 186 days after radiolabelling of the gold electrodes using a proton beam of a cyclotron accelerator, forming ^{195}Au isotopes. The radiolabel was stable since the radiolabel leaching rate in water was below detection limits.

Acknowledgments This work was partially funded by HMGU: EU FP7 Projects NeuroNano, NMP4-SL-2008-214547; ENPRA, NMP4-SL-2009-228789; InLiveTox, NMP4-SL-2009-228625; UBern: Swiss National Science Foundation Project 310030-120763; UBremen: S.P. and L.M. would like to thank National Science Foundation and the Environmental Protection Agency under Cooperative Agreement Number DBI-0830117 for supporting this work. Key support was also provided by the US Public Health Service Grants U19 ES019528 (UCLA Center for NanoBiology and Predictive Toxicology), RO1 ES016746, and RC2 ES018766. S.P. and L.M. would also like to thank Prof. A. Rosenauer and M. Schowalter, Department of Physics, University of Bremen, for TEM and EDX analysis.

References

Alessandrini F, Semmler-Behnke M, Jakob T, Schulz H, Behrendt H, Kreyling W (2008) Total and regional deposition of ultrafine particles in a mouse model of allergic inflammation of the lung. Inhal Toxicol 20(6):585–593

Arvizo R, Bhattacharya R, Mukherjee P (2010) Gold nanoparticles: opportunities and challenges in nanomedicine. Expert Opin Drug Deliv 7(6):753–763. doi:10.1517/17425241003777010

Baron PA, Willeke K (2001) Aerosol measurement: principles, techniques, and applications, 2nd edn. Wiley, New York

Baumeister W (2002) Electron tomography: towards visualizing the molecular organization of the cytoplasm. Curr Opin Struct Biol 12(5):679–684

Buffat P, Borel JP (1976) Size effect on the melting temperature of gold particles. Phys Rev A 13(6):2287–2298

Doane TL, Burda C (2012) The unique role of nanoparticles in nanomedicine: imaging, drug delivery and therapy. Chem Soc Rev 41(7):2885–2911. doi:10.1039/C2cs15260f

Donaldson K, Stone V, Tran CL, Kreyling W, Borm PJA (2004) Nanotoxicology. Occup Environ Med 61(9):727–728

Ferin J, Oberdörster G, Penney DP (1992) Pulmonary retention of ultrafine and fine particles in rats. Am J Respir Cell Mol Biol 6(5):535–542

Fierz M, Kaegi R, Burtscher H (2007) Theoretical and experimental evaluation of a portable electrostatic TEM sampler. Aerosol Sci Technol 41(5):520–528

Firestone RB, Ekström LP (2004) WWW table of radioactive isotopes. LBNL Isotopes Project—LUNDS Universitet, vol 2.1. Lund University, Lund, Sweden

Geiser M, Kreyling W (2010) Deposition and biokinetics of inhaled nanoparticles. Part Fibre Toxicol 7(1):2

Geiser M, Rothen-Rutishauser B, Kapp N, Schurch S, Kreyling W, Schulz H, Semmler M, Hof VI, Heyder J, Gehr P (2005) Ultrafine particles cross cellular membranes by nonphagocytic mechanisms in lungs and in cultured cells. Environ Health Perspect 113(11):1555–1560

Geiser M, Casaulta M, Kupferschmid B, Schulz H, Semmler-Behnke M, Kreyling W (2008) The role of macrophages in the clearance of inhaled ultrafine titanium dioxide particles. Am J Respir Cell Mol Biol 38(3):371–376

George S, Pokhrel S, Xia T, Gilbert B, Ji Z, Schowalter M, Rosenauer A, Damoiseaux R, Bradley KA, Madler L, Nel AE (2010) Use of a rapid cytotoxicity screening approach to engineer a safer zinc oxide nanoparticle through iron doping. ACS Nano 4(1):15–29. doi:10.1021/nn901503q

Gibson PN, Özsan ME, Lincot D, Cowache P, Summa D (2000) Modelling of the structure of CdS thin films. Thin Solid Films 361–362:34–40. doi:10.1016/s0040-6090(99)00833-0

Hainfeld JF, Slatkin DN, Focella TM, Smilowitz HM (2006) Gold nanoparticles: a new X-ray contrast agent. Br J Radiol 79(939):248–253

Holzwarth U, Bulgheroni A, Gibson N, Kozempel J, Cotogno G, Abbas K, Simonelli F, Cydzik I (2012) Radiolabelling of nanoparticles by proton irradiation: temperature control in nanoparticulate powder targets. J Nanopart Res 14(6):1–15. doi:10.1007/s11051-012-0880-y

Kreuter J (2004) Influence of the surface properties on nanoparticle-mediated transport of drugs to the brain. J Nanosci Nanotech 4(5):484–488

Kreyling W, Biswas P, Messing M, Gibson N, Geiser M, Wenk A, Sahu M, Deppert K, Cydzik I, Wigge C, Schmid O, Semmler-Behnke M (2011) Generation and characterization of stable, highly concentrated titanium dioxide nanoparticle aerosols for rodent inhalation studies. J Nanopart Res 13(2):511–524. doi:10.1007/s11051-010-0081-5

Kreyling WG, Semmler-Behnke M, Takenaka S, Möller W (2013) Differences in the biokinetics of inhaled nano-versus micrometer-sized particles. Accounts Chem Res (in press). doi:10.1021/ar300043r

Kuehl PJ, Anderson TL, Candelaria G, Gershman B, Harlin K, Hesterman JY, Holmes T, Hoppin J, Lackas C, Norenberg JP, Yu H, McDonald JD (2012) Regional particle size dependent deposition of inhaled aerosols in rats and mice. Inhal Toxicol 24(1):27–35. doi:10.3109/08958378.2011.632787

Liu Z, Kim SC, Wang J, Shin WG, Fissan H, Pui DYH (2012) Measurement of metal nanoparticle agglomerates generated by spark discharge using the universal nanoparticle analyzer (UNPA). Aerosol Sci Technol 46(3):333–346. doi:10.1080/02786826.2011.626002

Ma-Hock L, Gamer AO, Landsiedel R, Leibold E, Frechen T, Sens B, Linsenbuehler M, van Ravenzwaay B (2007) Generation and characterization of test atmospheres with nanomaterials. Inhal Toxicol 19(10):833–848

Maynard AD, Aitken RJ, Butz T, Colvin V, Donaldson K, Oberdörster G, Philbert MA, Ryan J, Seaton A, Stone V, Tinkle SS, Tran L, Walker NJ, Warheit DB (2006) Safe handling of nanotechnology. Nature 444(7117):267–269

Moghimi SM, Hunter AC, Murray JC (2005) Nanomedicine: current status and future prospects. FASEB J 19(3):311–330

Nel A, Xia T, Madler L, Li N (2006) Toxic potential of materials at the nanolevel. Science 311(5761):622–627

Nel AE, Mädler L, Velegol D, Xia T, Hoek EMV, Somasundaran P, Klaessig F, Castranova V, Thompson M (2009) Understanding biophysicochemical interactions at the nano-bio interface. Nat Mater 8(7):543–557

Oberdörster G, Oberdörster E, Oberdörster J (2005) Nanotoxicology: an emerging discipline evolving from studies of ultrafine particles. Environ Health Perspect 113:823–839

Papasani MR, Wang G, Hill RA (2012) Gold nanoparticles: the importance of physiological principles to devise strategies for targeted drug delivery. Nanomedicine (Lond). doi:10.1016/j.nano.2012.01.008

Peters A, Veronesi B, Calderon-Garciduenas L, Gehr P, Chen L, Geiser M, Reed W, Rothen-Rutishauser B, Schurch S, Schulz H (2006) Translocation and potential neurological effects of fine and ultrafine particles a critical update. Part Fibre Toxicol 3(1):13

Porter D, Sriram K, Wolfarth M, Jefferson A, Schwegler-Berry D, Andrew ME, Castranova V (2008) A biocompatible medium for nanoparticle dispersion. Nanotoxicology 2(3):144–154

Rand D, Ortiz V, Liu Y, Derdak Z, Wands JR, Tatíček M, Rose-Petruck C (2011) Nanomaterials for X-ray imaging: gold nanoparticle enhancement of X-ray scatter imaging of hepatocellular carcinoma. Nano Lett 11(7):2678–2683. doi:10.1021/nl200858y

Seaton A, Donaldson K (2005) Nanoscience, nanotoxicology, and the need to think small. Lancet 365(9463):923–924

Semmler-Behnke M, Kreyling WG, Lipka J, Fertsch S, Wenk A, Takenaka S, Schmid G, Brandau W (2008) Biodistribution of 1.4- and 18-nm gold particles in rats. Small 4(12):2108–2111. doi:10.1002/smll.200800922

Stoeger T, Reinhard C, Takenaka S, Schroeppel A, Karg E, Ritter B, Heyder J, Schulz H (2006) Instillation of six different ultrafine carbon particles indicates a surface area threshold dose for acute lung inflammation in mice. Environ Health Perspect 114(3):328–333

Takenaka S, Karg E, Kreyling WG, Lentner B, Möller W, Behnke-Semmler M, Jennen L, Walch A, Michalke B, Schramel P, Heyder J, Schulz H (2006) Distribution pattern of inhaled ultrafine gold particles in the rat lung. Inhal Toxicol 18(10):733–740

Takenaka S, Möller W, Semmler-Behnke M, Karg E, Wenk A, Schmid O, Stoeger T, Jennen L, Aichler M, Walch A, Pokhrel S, Mädler L, Eickelberg O, Kreyling WG (2012) Efficient internalization and intracellular translocation of inhaled gold nanoparticles in rat alveolar macrophages. Nanomedicine (Lond) 7:855–865. doi:10.2217/nnm.11.152

Wilson BJ (1966) The radiochemical manual, 2nd edn. Radiochemical Centre, Amersham

Zhang H, Ji Z, Xia T, Meng H, Low-Kam C, Liu R, Pokhrel S, Lin S, Wang X, Liao Y-P, Wang M, Li L, Rallo R, Damoiseaux R, Telesca D, Mädler L, Cohen Y, Zink JI, Nel AE (2012) Use of metal oxide nanoparticle band gap to develop a predictive paradigm for oxidative stress and acute pulmonary inflammation. ACS Nano 6(5):4349–4368. doi:10.1021/nn3010087